JOURNAL OF AIRCRAFT
Vol. 35, No. 1, January–February 1998

Motion Simulation Capabilities of Three-Degree-of-Freedom Flight Simulators

Nicolas A. Pouliot* and Clément M. Gosselin†
Université Laval, Québec, Quebec G1K 7P4, Canada
and
Meyer A. Nahon‡
University of Victoria, Victoria, British Columbia V8W 3P6, Canada

This paper presents the results of a study aimed at determining the simulation realism that might be achieved using reduced-degree-of-freedom flight simulator motion bases. More specifically, the quality of motion produced by two different three-degree-of-freedom platforms was compared to that produced by a conventional six-degree-of-freedom Stewart platform. The three-degree-of-freedom motion bases investigated were a spherical mechanism allowing only rotational motions, as well as a motion base capable of heave, pitch, and roll motions. To compare the different motion bases, three characteristic maneuvers were simulated using a nonlinear model of a Boeing 747. The aircraft motions were then simulated on nine different combinations of virtual motion platforms and motion base drive algorithms. The motion cues (specific forces and angular velocities) produced in this manner were then graphically compared. The analysis revealed that, in most cases, a three-degree-of-freedom simulator is capable of producing motion simulation quality comparable to that produced by a six-degree-of-freedom Stewart platform. Analysis of the motion sensations, as produced by a vestibular model, revealed nearly the same results as the motion analysis.

Introduction

THE six-degree-of-freedom Stewart platform is undoubtedly the most popular motion base for commercial flight simulators.[1] However, it is a complex and expensive mechanism that is best suited to full training simulators. Recently, there has been renewed interest in low-cost partial-training simulators that could be used for early pilot training, prior to the use of full-training simulators. As well, the advent of high-performance image generation (IG) systems[2] has decreased the relative importance of motion generation, thereby raising the issue of whether lower cost motion devices might be appropriate for full-training simulators. Finally, there has recently been heightened interest in lower-cost simulators for application to road vehicle simulation, entertainment, and virtual reality systems. Relatively little work exists in the area of the design of reduced-degree-of-freedom (DOF) motion bases or in the evaluation of the quality of motion sensations that could be produced by these devices.[3–5]

The purpose of this paper is to analyze the simulation realism that can be achieved using alternative motion base mechanisms, with only three degrees of freedom. It is conjectured that this reduced motion capability might provide a cheaper alternative to existing designs (simplicity, reduced cost of manufacturing, and operation) while still producing good quality motion simulation for large transport aircraft. In all, nine combinations of motion base architecture and drive algorithms were evaluated using three different aircraft maneuvers. The evaluation maneuvers used in this study were chosen to ensure that a limited number of maneuvers would provide a broad range of motions, including both low- and high-frequency accelerations in all DOFs.

Presented as Paper 96-3474 at the AIAA Flight Simulation Technologies Conference, San Diego, CA, July 29–31, 1996.

*Graduate Student, Département de Génie Mécanique. E-mail: pouliot@gmc.ulaval.ca. Student Member AIAA.

†Professor, Département de Génie Mécanique. E-mail: gosselin@gmc.ulaval.ca. Member AIAA.

‡Associate Professor, Department of Mechanical Engineering. E-mail: mnahon@me.uvic.ca. Senior Member AIAA.

Background Material

Type of Aircraft and Modeling

The present work focuses on the simulation of commercial airliners; the Boeing 747 has been chosen as a typical example. This emphasis is because of the Boeing 747's large inertia: the natural motion of these aircraft lends itself well to motion simulations that are principally composed of low-frequency rotations (including tilt coordination). Thus, high-frequency translational accelerations such as those required for the simulation of military aircraft would tend to be poorly simulated by the alternative platforms considered here. A complete nonlinear model of the Boeing 747 (Refs. 6 and 7) is used in the present work to predict aircraft motion in response to a range of pilot inputs. The reference frames associated with the aircraft are shown in Fig. 1a.

F_{Ia} is the inertial reference frame, fixed to the ground. By convention, the Z axis points vertically downward, and the X axis is parallel to the active runway. A second reference frame, F_a, is attached to the aircraft and has its origin at the c.m. of the aircraft CG_a. The X axis of F_a points longitudinally forward, while the Z axis points downward with respect to the aircraft. As a result, the Y axis points out the right wing. Furthermore, $\boldsymbol{S}_{a1}$ is defined as the vector connecting the origin of frame F_{Ia} to the origin of frame F_a (Fig. 1a). Finally, Euler angles, denoted by the ordered triple $\beta_a = \{\phi_a, \theta_a, \psi_a\}$, are used to specify the relative orientation of frame F_a with respect to the inertial frame F_{Ia}. Hence, the inertial position of a point of the aircraft whose position vector with respect to frame F_a is given by $[\boldsymbol{P}]_{F_a}$ can be written as

$$[\boldsymbol{P}]_{F_{Ia}} = [\boldsymbol{S}_{a1}]_{F_{Ia}} + \boldsymbol{Q}_a[\boldsymbol{P}]_{F_a} \tag{1}$$

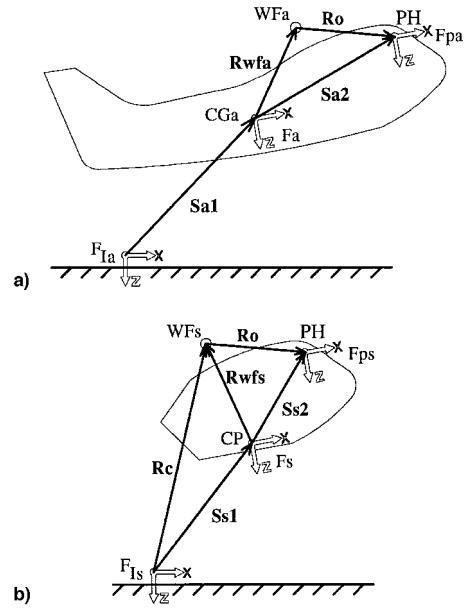

Fig. 1 a) Aircraft's and b) simulator's reference frames.

where

$$\boldsymbol{Q}_a = \begin{bmatrix} c\theta_a c\psi_a & s\phi_a s\theta_a c\psi_a - c\phi_a s\psi_a & c\phi_a s\theta_a c\psi_a + s\phi_a s\psi_a \\ c\theta_a s\psi_a & s\phi_a s\theta_a s\psi_a + c\phi_a c\psi_a & c\phi_a s\theta_a s\psi_a - s\phi_a c\phi_a \\ -s\theta_a & s\phi_a c\theta_a & c\phi_a c\theta_a \end{bmatrix} \tag{2}$$

where c stands for cos( ) and s for sin( ). The relationship between the time derivatives of the Euler angles and the angular velocity vector of the aircraft $\boldsymbol{\omega}_a$ is then written as

$$\boldsymbol{\omega}_a = \boldsymbol{R}_a \dot{\beta}_a \quad \text{where} \quad \boldsymbol{R}_a = \begin{bmatrix} 1 & 0 & -s\theta_a \\ 0 & c\phi_a & s\phi_a c\theta_a \\ 0 & -s\phi_a & c\phi_a c\theta_a \end{bmatrix} \tag{3}$$

and $\dot{\beta}_a$ is the time derivative of β_a.

A third reference frame, denoted F_{Pa}, having the same orientation as F_a is also defined, with its origin at the center of the pilot's head (PH). The vector connecting the origins of these two frames, $\boldsymbol{S}_{a2}$, is illustrated in Fig. 1a. In the present study, this vector has been assigned the value $\boldsymbol{S}_{a2} = [26.2 \; -0.465 \; -3.4]^T$ m, which approximately represents the pilot's head location in a Boeing 747.

The reference frames associated with the simulator's motion base are shown in Fig. 1b. An inertial reference frame F_{Is} is fixed to ground, directly below the center of the simulator's motion base, when the simulator is in its neutral position. Moreover, frames F_s and F_{Ps} are attached to the moving platform of the simulator with their origins located at the geometric center of the simulator's moving platform CP and at the center of the pilot's head PH, respectively. The latter frames have the same orientation, which is given by the simulator's Euler angles, using the convention defined for the aircraft. Finally, $\boldsymbol{S}_{s1}$ is defined as the vector connecting F_{Is} to F_s, and $\boldsymbol{S}_{s2}$ is defined as the vector connecting F_s to F_{Ps}. By using the simulator's Euler angles values, one can define the matrices $\boldsymbol{Q}_s$ and $\boldsymbol{R}_s$ with equations similar to Eqs. (2) and (3). Other points and vectors shown in Fig. 1 will be defined later.

Human Vestibular System and Model

The purpose of defining a reference frame with its origin at the pilot's head is to allow the determination of the sensations that he or she would experience in the aircraft or simulator. Although several motion sensors in the human body contribute to the detection of motion, the part of the inner ear referred to as the vestibular system plays a dominant role in motion sensing activities.[8] Furthermore, it is generally accepted that the cues sensed by the vestibular system are the specific forces $\boldsymbol{f}$ and angular velocities $\boldsymbol{\omega}$ to which the human is subjected. The former are sensed by the otolith, while the latter are sensed by the semicircular canals.

It is recalled that the specific force is a vectorial quantity defined as the difference between the translational acceleration vector $\boldsymbol{a}$ and the gravitational acceleration vector $\boldsymbol{g}$, i.e., $\boldsymbol{f} = \boldsymbol{a} - \boldsymbol{g}$. Hence, a body at rest under the action of the Earth's gravitational field is said to be experiencing an upward specific force of 9.81 m/s^2, in the negative direction of the Z axis defined earlier.

A mathematical model of the vestibular system was used in this study to evaluate the motion sensations that a pilot would experience in the real aircraft or in the flight simulator, thereby allowing an objective comparison. The model accepts as inputs the components of vectors $\boldsymbol{f}$ and $\boldsymbol{\omega}$, processes them independently, and then outputs six new components, referred to as the sensed specific forces $\boldsymbol{f}'$ and sensed angular velocities $\boldsymbol{\omega}'$. The processing roughly consists of a bandpass frequency filter window, admitting frequencies of 0.2–2 rad/s for the $\boldsymbol{f}$ components and 0.2–10 rad/s for the $\boldsymbol{\omega}$ components. Threshold values, ranging from 0.17 to 0.28 m/s^2 for linear accelerations and from 2.6 to 3.6 deg/s for the angular velocities, below which no motion is sensed, have also been suggested, based on tests of pilots in typical flying tasks.[9] A complete description of the vestibular models used in the present work, as well as the details of their implementation, can be found in Reid and Nahon.[10]

Washout Filter Algorithm

Because the flight simulator motion base has a limited range of motion, it is not possible to exactly reproduce the angular velocities and specific forces experienced in the aircraft. Hence, motion generation algorithms (washout filters) have been developed to generate the best motion commands within the constraints of the motion system. The principles of the washout algorithm used in the present work will now be reviewed.

One of the most demanding tasks for a motion base with limited motion travel is the reproduction of low-frequency translational accelerations. For example, a constant acceleration of 1 m/s^2 along the X axis sustained for 5 s would require a travel of 12.5 m. However, it is also possible to slowly tilt the simulator about its Y axis at an angle of approximately 6 deg, while the visual display continues showing horizontal flight conditions. The pilot would then experience a specific force component along the X axis of $9.81 \cdot \sin(6 \text{ deg}) \simeq 1$ m/s^2. Although the Z component of the specific force experienced by the pilot would then be reduced to 9.75 m/s^2, this change should not be noticeable if the tilt rate is below the threshold value. The effectiveness of this process, known as tilt coordination, to simulate low-frequency translational accelerations leads to an increased importance of the rotational channels in relation to the translational channels.

The washout filter (WF), which includes the previously mentioned tilt coordination, receives as inputs the specific forces and angular velocities sampled at a particular location in the aircraft, referred to as the washout location and denoted WF$_a$ and WF$_s$ in Fig. 1, and outputs the optimum displacement vector ($\boldsymbol{R}_C$) and the Euler angles β_s that the simulator's cockpit should assume. The WF also continually tries to return the motion platform to the central location of its range of motion (the neutral point).

There exist several variations of WF algorithms,[11] but its classical form has been used here because of its widespread use in commercial simulators. A complete description of this algorithm can be found in Nahon et al.,[10,12,13] while Fig. 2 illustrates the algorithm as used in the present work. The dashed-line block denoted as HF emulator is an addition de-

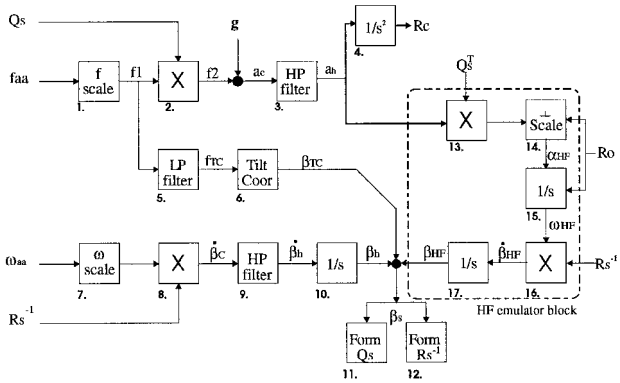

Fig. 2 Washout filter algorithm layout.

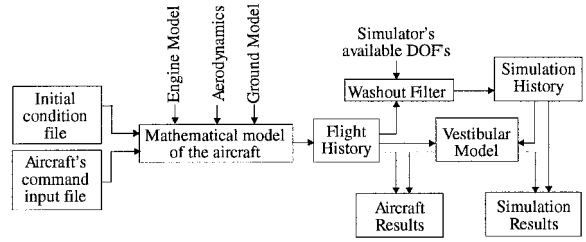

Fig. 3 Layout of the methodology.

veloped for the purposes of the present work only and will be described in a subsequent section. Consequently, boxes 13–17 are nonexistent in the conventional classical WF algorithm.

As seen in Fig. 2, the washout algorithm is broadly divided into three parallel channels of motion. The upper channel (translational), consisting of boxes 1–4, scales the input specific forces $\boldsymbol{f}_{aa}$, transforms the resulting vector into the inertial reference frame, and then adds the gravity vector. This produces the acceleration vector $\boldsymbol{a}_c$, which must be filtered to extract only its high-frequency component $\boldsymbol{a}_h$ to assure that the simulator will remain near its neutral point. Finally, $\boldsymbol{a}_h$ is integrated twice to obtain the required displacements of the platform $\boldsymbol{R}_C$. The bottom channel (rotational), consisting of boxes 7–10, is similar to the translational channel but acts upon angular velocities. Hence, box 10 only carries out a single integration, thus producing a set of Euler angles β_h. The central channel, consisting of boxes 5 and 6, represents tilt coordination. Box 5 receives the scaled specific forces and extracts their low-frequency components that are then transformed by box 6 into tilt angles β_{TC}. Box 6 also includes a rate limiter to ensure that the tilt coordination will occur slowly enough to keep the effect realistic. The sum of β_h and β_{TC} provides β_s, the orientation of the simulator, which is then used to compute the matrices $\boldsymbol{Q}_s$ and $\boldsymbol{R}_s$. Strictly speaking, the direct summation of β_h and β_{TC} will introduce some error because these are not true vectors (they are ordered triples). However, this structure of the washout algorithm has been shown to be effective,[14] and, for the purposes of the present work, the use of a proven washout algorithm was considered of paramount importance.

In this study, a scale factor of 1.0 was used in boxes 1 and 7. However, scale factors closer to 0.75 are more typical in commercial simulators to help keep the excursion of the platform within its physical limits.

Methodology

In this work, aircraft simulation software developed at the University of Toronto Institute for Aerospace Studies (UTIAS) to drive a full-scale six-degree-of-freedom simulator[10] was used off-line on a workstation. Some of the algorithms included in the software were modified to simulate the three-degree-of-freedom motion bases evaluated in this work. Indeed, it is possible to artificially reduce the simulator's number of degrees of freedom (DOF) by inhibiting, for instance, all of the translations while keeping the rotational motion, thus emulating the behavior of a three-degree-of-freedom spherical simulator.

Figure 3 summarizes the various steps required to produce the results. The primary inputs consist of two standard text files. The first data file supplies the initial conditions necessary to solve the differential equations of flight. The second data file is a complete time history of the aircraft's control inputs (elevator deflection, throttle position, wheel angle, etc.) for the entire simulated maneuver with a sampling frequency of 20 Hz. The aircraft model, with the help of three major modules (engine model, aerodynamic, and ground model), then outputs the simulated flight history to a file. The specific forces and angular velocities thus obtained are then fed directly into the vestibular model and into the WF algorithm. As depicted in Fig. 3, the WF transforms the flight history into the simulator motion time history, according to which degrees of freedom are currently available. Finally, the simulator specific forces and angular velocities are fed into the vestibular model, which processes both the aircraft and simulator flight histories to produce the pilot sensations time histories.

The methodology described in the preceding text produces results that can be used to compare the quality of the motion simulation obtained with three-degree-of-freedom and six-degree-of-freedom simulators. Additionally, the results obtained with both types of simulator can also be compared with the real flying experience.

Table 1 Aircraft initial conditions

Initial conditions file	Runway	Cruise
Speed, m/s	50.0	212.5
Altitude, m	4.67	6280
Engine pressure ratio	1.02	1.10

Evaluation Maneuvers

Because it would not be possible to test an exhaustive set of aircraft flying sequences, a limited number of maneuvers had to be selected. Three characteristic maneuvers were used to perform the comparison between the simulators. These maneuvers were chosen to exercise the full range of simulator DOFs.

The first maneuver started with the initial conditions referred to as runway conditions, while the others started with the in-flight cruise conditions. These initial conditions are summarized in Table 1. A brief description of each of the three maneuvers follows.

Take-Off Maneuver

This take-off maneuver (TOM) begins at a speed of 50 m/s on the runway with the throttle lever at 15% of maximum power. After 3 s, the throttle is abruptly set to 100% and the aircraft accelerates. At $t = 11$ s, when rotation speed is reached, the nose is lifted and soon after the aircraft takes off at a steady pitch angle of 10 deg. Finally, 6 s later, a sudden failure occurs on the right outboard engine and the pilot eases the elevator to keep the aircraft level. The maneuver ends at $t = 25$ s.

Turn-Entry Maneuver

In this 40-s turn-entry maneuver (TEM), the aircraft, flying at cruise condition, first rolls right, then left, and then right again. The maximum bank angle in each roll is approximately 40 deg. The pilot adjusts the elevator to keep the aircraft's altitude almost constant, and the throttle lever is set at 55% of maximum power for the entire maneuver.

Throttle Impulse Maneuver

The pilot, initially flying at a cruise condition with 55% power, suddenly increases the throttle setting to maximum power while adjusting the elevator to keep the aircraft's altitude constant. Seventeen seconds later the throttle is set to idle until the end of the throttle impulse maneuver (TIM), at $t = 40$ s.

The time history of the aircraft's control inputs defining these maneuvers was based on control time histories recorded in the UTIAS simulator while working with professional pilots.[14] All maneuvers were run without atmospheric turbulence.

Location of Washout

The original washout filter software taken from Reid and Nahon[10] performed the washout calculations using values of specific forces existing at the location in the aircraft corresponding to the centroid of the motion base. However, the present work also investigated alternative washout locations. As shown in Fig. 1, the location of WF_a (and WF_s), at which washout is performed, is defined with respect to the pilot's head by means of $\boldsymbol{R}_0$. Preliminary tests indicated that it was imperative that $\boldsymbol{R}_0$ be identical in both the aircraft and the simulator, i.e., that WF_a and WF_s be in the same location relative to the pilot's head. Attempts to use other configurations invariably led to the generation of unwanted spurious translational accelerations.

However, to compute the hydraulic cylinder lengths, the kinematics transformation software requires the position of the centroid of the motion base, denoted by CP in Fig. 1, to be specified. To accomplish this, even when washout might not be performed at CP, vector $\boldsymbol{R}_{WF_s}$ must be calculated according to $\boldsymbol{R}_{WF_s} = \boldsymbol{S}_{s2} - \boldsymbol{R}_0$, where $\boldsymbol{S}_{s2} = [-0.002 \; -0.465 \; -1.783]^T$ m, expressed in frame F_s. This value for $\boldsymbol{S}_{s2}$ represents the pilot's head location relative to the centroid of the moving platform for the UTIAS flight simulator.

Three locations for the washout filter were thus evaluated in the present work:

1) *The pilot's head (PH)*: In this case we set $\boldsymbol{R}_0 = [\,0\;0\;0]^T$ and $\boldsymbol{R}_{WF_s} = \boldsymbol{S}_{s2}$. The benefit of this scenario is that no spurious translational accelerations are generated at the pilot's head.

2) *Centroid of the platform (CP)*: We then have $\boldsymbol{R}_0 = \boldsymbol{S}_{s2}$ and $\boldsymbol{R}_{WF_s} = [0\;0\;0]^T$. This is the usual convention, as used in Reid and Nahon.[10]

3) *Center of gravity of the simulator (CG)*: For the UTIAS simulator, this location has been approximated as $\boldsymbol{R}_0 = [-0.02 \; -0.465 \; -0.483]^T$ m. The benefit of this location is that it tends to minimize the dynamic actuation forces, because off-center rotations are not generated.

Alternative Motion Base Architectures

In the present work, three different motion base architectures were simulated and compared. The last two use a particular combination of three degrees of freedom that could be emulated using a real six-degree-of-freedom simulator.

Stewart Platform

The first architecture is the conventional Stewart platform (STW) that possesses a full six degrees of freedom. It can translate along all three orthogonal directions independently, as well as rotate about these same axes. A schematic representation of this motion base is shown in Fig. 4a. At a given time step, the washout filter algorithm produces $\boldsymbol{R}_C$ and the orientation matrix $\boldsymbol{Q}_s$.

Spherical Platform

The second architecture considered has only three degrees of freedom, consisting of rotations about three mutually perpendicular axes. Figure 4b shows a representation of what the motion base [spherical (SPH)] might look like. As highlighted in the discussion of tilt coordination, the rotational motion channels are particularly important in the simulation of large transport aircraft. Because the platform is only capable of rotations, the only useful ouput from the washout algorithm is $\boldsymbol{Q}_s$, and the linear displacements are systematically set to zero. The location at which washout is performed (WF_s) will thus remain fixed.

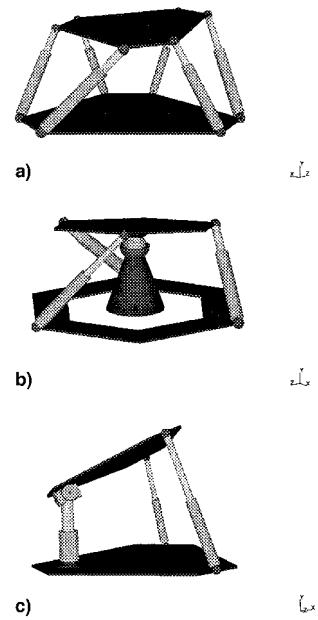

Fig. 4 Different motion base architectures: a) STW, b) SPH, and c) HPR.

Heave-Pitch-Roll Platform

The third architecture [heave-pitch-roll (HPR)] also has three degrees of freedom, but this time including translation along the vertical axis (heave). The other two degrees of freedom consist of rotations about the two horizontal axes, namely the pitch (about the Y axis) and roll (about the X axis). The notation HPR therefore stands for Heave-Pitch-Roll. Figure 4c shows a representation of what this motion base might look like. The point WF_s will be constrained to move along a vertical axis while the two rotations are performed about this point. In this case, the useful output of the washout filter are the Z component of $\boldsymbol{R}_C$ and the roll and pitch components of β_s.

High-Frequency Emulator

To compensate for the loss of translational motion in the three-degree-of-freedom SPH and HPR architectures, a further modification of the washout algorithm, called a high-frequency (HF) emulator, was evaluated. Its purpose is to reproduce some of the high-frequency translational accelerations by commanding an appropriate angular acceleration, assuming that the pilot's head is displaced from the center of rotation by a nonzero vector $\boldsymbol{R}_0$. The HF emulator, consisting of boxes 13–17 in Fig. 2, was thus incorporated into the washout filter algorithm and is described next.

First, assume that the high-frequency acceleration that must be emulated is denoted by $\boldsymbol{a}_h$. This acceleration can be transformed into the simulator reference frame according to $\boldsymbol{a} = \boldsymbol{Q}_s^T \boldsymbol{a}_h$. Because an angular acceleration can only produce translational accelerations that are perpendicular to $\boldsymbol{R}_0$, the following transformation is performed on $\boldsymbol{a}$ to remove the acceleration component along $\boldsymbol{R}_0$:

$$\boldsymbol{a}_\perp = \boldsymbol{a} - (\boldsymbol{a} \cdot \boldsymbol{R}_0) \frac{\boldsymbol{R}_0}{\|\boldsymbol{R}_0\|^2} \tag{4}$$

The resulting vector now represents the component of the original high-frequency acceleration that is possible to emu-

Table 2 Studied architectures

	@PH	@CP	@CG	+HF
STW (six-degree-of-freedom)	•	•	——	——
SPH (three-degree-of-freedom)	•	•	•	•
HPR (three-degree-of-freedom)	•	•	——	•

Table 3 STW motion base travel limits

Linear	Angular
$X \pm 0.65$, m	$\phi \pm 20.8$, deg
$Y \pm 0.59$, m	$\theta \pm 21.3$, deg
$Z \pm 0.52$, m	$\psi \pm 20.0$, deg
v_{max} 0.80, m/s	ω_{max} 34.4, deg/s
a_{max} 10.0, m/s^2	α_{max} 400, deg/s^2

late. A corresponding angular acceleration can then be calculated according to

$$\boldsymbol{\alpha}_{HF} = \frac{\|\boldsymbol{a}_\perp\|}{\|\boldsymbol{R}_0\|}\frac{(\boldsymbol{R}_0 \times \boldsymbol{a}_\perp)}{\|(\boldsymbol{R}_0 \times \boldsymbol{a}_\perp)\|} = \frac{(\boldsymbol{R}_0 \times \boldsymbol{a}_\perp)}{\|\boldsymbol{R}_0\|^2} \tag{5}$$

That value can be integrated once to obtain $\boldsymbol{\omega}_{HF}$, then multiplied by the inverse of the $\boldsymbol{R}_s$ matrix to obtain the Euler angles rates $\dot{\beta}_{HF}$, which are finally integrated to yield β_{HF}.

When the HF emulator is to be used with the three-degree-of-freedom SPH motion base, $\boldsymbol{R}_0$ is set to $[1.25\ 0\ 0]^T$, representing a center of rotation located behind the pilot, and allowing mainly Y and Z accelerations to be emulated. When the HF emulator is used with the three-degree-of-freedom HPR motion base, $\boldsymbol{R}_0$ is set to $[0\ 0\ -1.25]^T$, because high-frequency vertical accelerations need not be emulated (they can be produced directly by the motion base). The HF emulator is automatically disabled when using the six-degree-of-freedom STW motion base.

Table 2 summarizes the nine different combinations of motion bases, washout filter locations, and HF emulator that were used in this study for each of the three maneuvers. A total of 27 sets of results were therefore generated and will be presented in the Results and Discussion section.

Conservative Assumptions

Additional assumptions were made to ensure that this study would remain conservative. The first was to assume that all three motion bases would have the same range of motion capabilities for those DOFs that were active. This assumption was dictated by the need to allow a future comparison to be performed on a standard six-degree-of-freedom motion base. Table 3 shows the assumed motion limits, taken from Reid and Nahon.[14] Note, however, that a three-degree-of-freedom motion base could likely be designed to have a much wider range of angular travel and of velocities than the Stewart platform.

A second conservative assumption was to use the same washout filter structure and coefficients for all motion bases (except for the HF emulator, when active). This washout filter had been designed to give good performance on the six-degree-of-freedom motion base described in Table 3. It should be noted, however, that the washout filter algorithm could likely be improved for operation with a specific three-degree-of-freedom motion base.

Results and Discussion

Performance Indicators

The 27 sets of results mentioned in the preceding text, produced by using different combinations of evaluation maneuver, motion base architecture, washout filter location, and HF emulator, were evaluated in a number of ways. The initial results were generated as time histories of different variables. These included pilot control inputs, aircraft and simulator positions, velocities and accelerations, pilot vestibular model responses, and motion base actuator lengths. From these results, 12 graphs were then constructed for each set: three for the components of the specific force $\boldsymbol{f}$; three others for the corresponding sensed specific forces $\boldsymbol{f}'$; three for the components of the angular velocity $\boldsymbol{\omega}$; and three more for the sensed angular velocities $\boldsymbol{\omega}'$. On each graph, three curves were plotted: the first representing the aircraft's values, the second denoting the simulator's values, and the third giving the difference between the first two.

These results were then examined visually. However, because this type of evaluation would clearly be subjective, complementary objective comparison tools, called performance indicators, were also devised. The first of these indicators, λ_1, is intended to yield a single numerical value describing the average error between motion cues generated in the aircraft and those produced in a simulator, while the second indicator, λ_2, describes the average error in the rate of change of the same variables. The two indicators, aimed to be invariant, are described by the following equation, in which $i \in \{1, 2\}$:

$$\lambda_i = 100 \times \left(\frac{\lambda_{if}}{a_{max}} + \frac{\lambda_{i\omega}}{\omega_{max}}\right) \tag{6}$$

Each performance indicator is a weighted average of six component indicators, corresponding to the six motion channels. Moreover, because translational quantities have different unit dimensions than angular ones, all quantities were normalized by their corresponding upper limits a_{max} and ω_{max} taken from Table 3.

The component indicators that make up λ_1 are defined as follows:

$$\lambda_{1f} = \frac{1}{\mathcal{F}T}\sum_{j=0}^{\mathcal{F}T}\sqrt{(f_{xj} - f_{xj}^{sim})^2 + (f_{yj} - f_{yj}^{sim})^2 + (f_{zj} - f_{zj}^{sim})^2} \tag{7}$$

$$\lambda_{1\omega} = \frac{1}{\mathcal{F}T}\sum_{j=0}^{\mathcal{F}T}\sqrt{(\omega_{xj} - \omega_{xj}^{sim})^2 + (\omega_{yj} - \omega_{yj}^{sim})^2 + (\omega_{zj} - \omega_{zj}^{sim})^2} \tag{8}$$

where, for example, f_{kj} is the k component of $\boldsymbol{f}$ taken at the instant $t = j\Delta t$.

Thus, we evaluated the magnitude of the error at the instant $t = j\Delta t$ between the specific force (or angular velocity) experienced in the aircraft and in the simulator. This magnitude was then summed over the complete maneuver, of duration T, and normalized by T and by the sampling frequency $\mathcal{F}$ (20 Hz), that is, by the total number of elements in the summation.

The second performance indicator, λ_2, quantifies the difference between the derivative of the simulator and aircraft specific forces (and angular velocities) and is defined as

$$\lambda_{2f} = \frac{1}{(\mathcal{F}T - 1)}\sum_{j=1}^{\mathcal{F}T}\sqrt{\delta\dot{f}_{xj}^2 + \delta\dot{f}_{yj}^2 + \delta\dot{f}_{zj}^2} \tag{9}$$

$$\lambda_{2\omega} = \frac{1}{(\mathcal{F}T - 1)}\sum_{j=1}^{\mathcal{F}T}\sqrt{\delta\dot{\omega}_{xj}^2 + \delta\dot{\omega}_{yj}^2 + \delta\dot{\omega}_{zj}^2} \tag{10}$$

where, for each $k \in \{x, y, z\}$:

$$\delta\dot{f}_{kj} = \frac{\Delta f_{kj}}{\Delta t} - \frac{\Delta f_{kj}^{sim}}{\Delta t} \tag{11}$$

$$\delta\dot{\omega}_{kj} = \frac{\Delta \omega_{kj}}{\Delta t} - \frac{\Delta \omega_{kj}^{sim}}{\Delta t} \tag{12}$$

where, for example, $\Delta f_{kj} = f_{kj} - f_{k(j-1)}$. Thus, the derivative of the specific force $\Delta f_{kj}/\Delta t$ (or of the angular velocity, $\Delta\omega_{kj}/\Delta t$) component is evaluated at time $t = j\Delta t$ using a first backward difference, where Δt is $1/\mathcal{F} = 0.05$ s. The error in this quantity is taken as the difference between aircraft's and simulator's values. These are then squared and summed over the duration of the maneuver and normalized by $(\mathcal{F}T - 1)$, because the summation now begins at $t = \Delta t$.

Graphical Examples

Ten plots are now presented to illustrate the results obtained (Fig. 5). These are a condensed version of the plots previously mentioned, for the sake of compactness. Four curves now appear on each plot: a fine dotted line shows the aircraft's behavior; a coarser dotted line represents the behavior of the six-degree-of-freedom STW; a solid curve shows the behavior of the three-degree-of-freedom platform under consideration; and finally, a dashed line shows the difference between the two simulators (six-degree-of-freedom and three-degree-of-freedom). Graphs 5b and 5d show a component of the sensed specific force as evaluated by the vestibular model from the corresponding specific force plotted in graphs 5a and 5c. The same vertical scaling has been used for both graphs to emphasize the amplitude reduction, whereas the shadowed region represents the range of specific forces within the threshold values. No angular velocity plots have been presented in this paper because most of the three-degree-of-freedom architectures considered produce exactly the same motions as the six-degree-of-freedom platform: only the yaw axis of HPR motion bases and the HF emulator produced different angular time histories.

Takeoff Maneuver

Early in this maneuver, the aircraft is subjected to a relatively large-amplitude, low-frequency longitudinal acceleration as the aircraft accelerates down the runway. Later in the maneuver, at $t = 17$ s, a high-frequency motion is apparent when the engine failure occurs.

Figure 5a shows the X-specific force produced by the six-degree-of-freedom STW@PH and the three-degree-of-freedom SPH@PH simulations. Tilt coordination begins at $t = 3$ s in both cases. However, the tilt-coordination rate limit (of 3 deg /s) prevents both simulators from producing an X-specific force buildup that is as rapid as in the aircraft. When the nosewheel is rotated (at $t = 11$ s), the tilt angle is further increased in both simulators to produce a larger X-specific force. The circled region highlights the weakness of the SPH@PH in producing a high-frequency acceleration at the instant the engine fails, whereas the STW@PH manages to quickly reduce the X-specific force in the same direction as the aircraft (though not to the same extent), the spherical motion base is constrained by the low-frequency nature of its tilt coordination. This difference is clearly visible in the Δf_X curve.

However, Fig. 5b shows that the vestibular processing smooths the curves shown in Fig. 5a, making the engine failure deviation between the three-degree-of-freedom and the six-degree-of-freedom results almost vanish. In fact, because the sensation differences are all below threshold values, it is likely that differences between the simulations will be undetectable by the pilot. This presumes that the resolution of the vestibular apparatus is similar to its sensation thresholds, so that two sensations that differ by less than the threshold will not be detected as being appreciably different.

In a separate test with the same maneuver, the Z-specific forces produced by a six-degree-of-freedom STW@PH motion base and by the three-degree-of-freedom SPH + HF motion base are shown in Fig. 5c. From this plot, it becomes clear that both simulators do a poor job of simulating this channel of motion. The reason is that tilt coordination cannot be called upon to produce any vertical acceleration. Furthermore, in the attempt to generate a longitudinal specific force, any platform

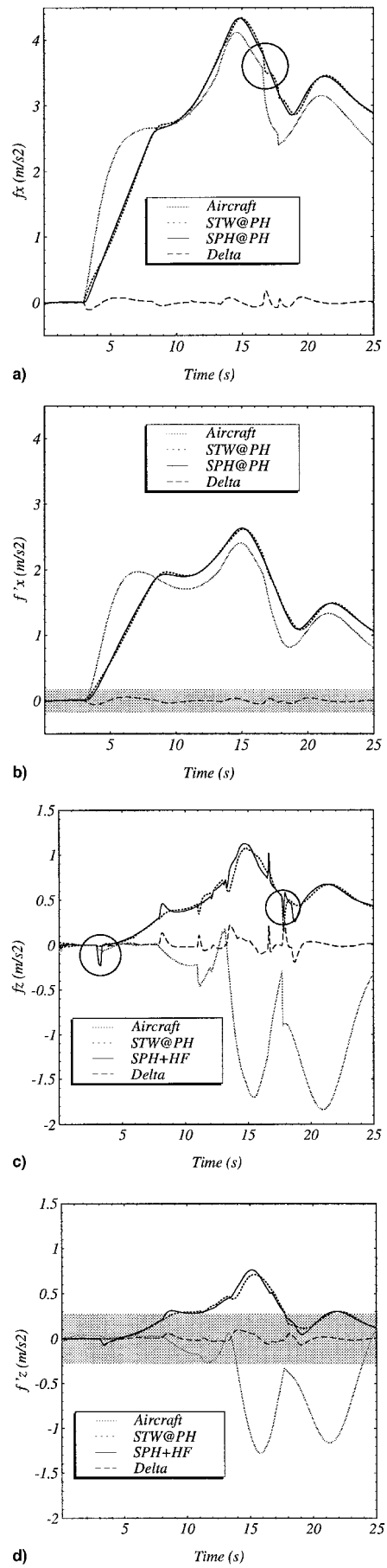

Fig. 5 Specific forces generated in the TOM: a) x component of f, b) x component of f', c) z component of f, and d) z component of f'.

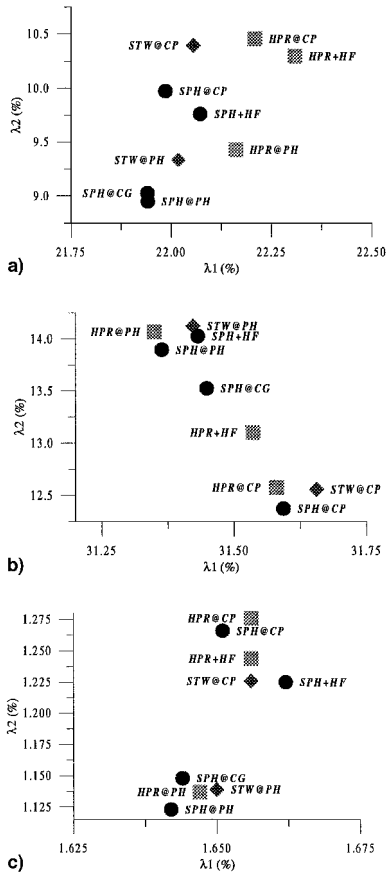

Fig. 6 Performance indices obtained for each of the maneuvers. λ_i in a) TOM, b) TEM, and c) TIM.

will invariably be constrained to generate positive (downward) values of f_Z. The first circled region in this plot shows a sudden deviation of the SPH + HF from the STW, which is because of the position of the pilot with respect to the center of rotation ($\boldsymbol{R}_0$). As a result of this displacement, when the tilt-coordination process begins, the pilot is subjected to an upward acceleration. The second circled region highlights an area where the HF emulator produces a beneficial effect. Figure 5d presents the sensed vertical specific force, which is substantially smoother than f_Z. Very little vertical specific force will be sensed by the pilot because the curve is covered by the gray area during most of the maneuver. These and other graphical results for the TOM confirm that the spherical motion base appears almost as effective as the Stewart platform in this maneuver. In particular, the SPH@PH and SPH@CG architectures produce results that are especially close to the STW@PH curves. HPR architectures also performed relatively well, especially in the *Z*-linear channel of motion. However, their weakness showed up when the yaw channel was considered, because no rotational motion is possible for them in this direction, although it is needed during the engine-failure segment of the simulation.

This analysis is confirmed, for TOM, by the values of the performance indices λ_1 and λ_2, as shown in Fig. 6a, where each combination studied is represented in a two-dimensional space. On this plot, the best performing combinations are those located nearest the origin of the coordinate system. However, there is a relatively small difference (about 0.5%) between all of the combinations.

TEM

This maneuver is the only one in which relatively large-amplitude translational accelerations and angular velocities are generated in all three channels of motion for the entire duration

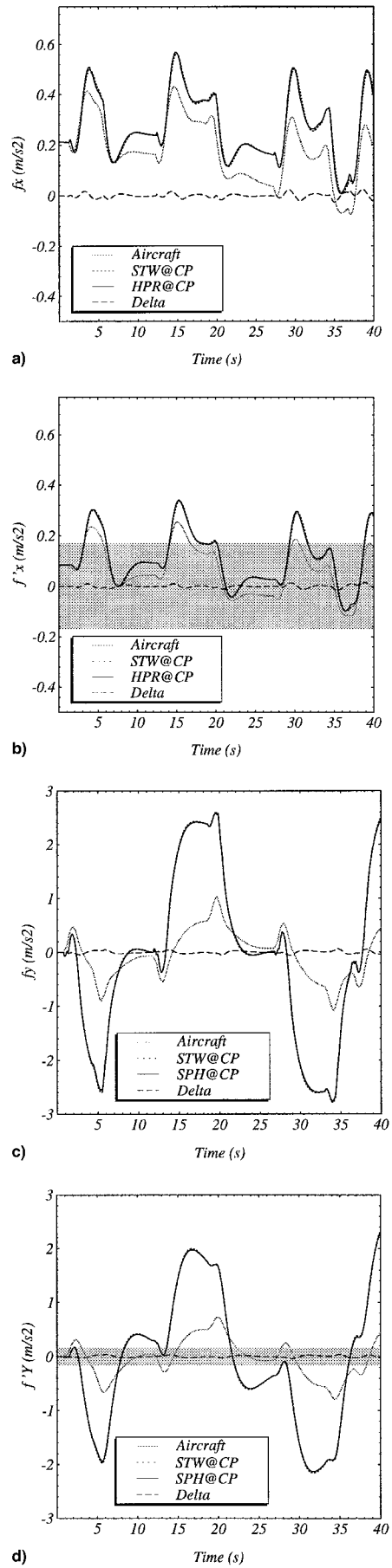

Fig. 7 Specific forces generated in the TEM: a) *x* component of *f*, b) *x* component of *f′*, c) *y* component of *f*, and d) *y* component of *f′*.

of the maneuver. Figures 7a and 7b, respectively, show the f_X and f'_X motion channels as they are simulated by STW@CP and HPR@CP. The near-zero Δf_X curve shows that the three-degree-of-freedom simulation is almost identical to the six-degree-of-freedom simulation. The angular velocities produced by both of these simulators are identical, except in yaw. Once again, the shadowed area of the threshold value covers most of the f'_X curve. By contrast, the simulation of lateral specific force is much poorer, as shown in Figs. 7c and 7d, where the SPH@CP architecture is used as a case in point. It is clear from Fig. 7 that during this maneuver there is a large difference between the amplitude of aircraft's lateral specific force f_Y and that experienced in both simulators. This is because the aircraft tends to produce near-coordinated turns, i.e., the centripetal acceleration compensates for the lateral component of the gravity vector induced by the bank angle. The simulators, on the other hand, have no way of compensating for the lateral specific force produced by the bank angle, and the similarity between the performance of a three-degree-of-freedom simulator and a six-degree-of-freedom simulator is again clearly visible, i.e., they are both equally poor.

Once again, the f_Z specific force was poorly reproduced in most cases, including the Stewart platform. The simulator motion produced for this maneuver was nearly the same for all nine architectures considered and hardly differed for the three-degree-of-freedom and six-degree-of-freedom simulators. Based on a visual inspection of their results, SPH@CP, SPH@CG, and HPR@CP seemed to produce the best motion of the three-degree-of-freedom motion bases.

The analysis of Fig. 6b reveals that all of the studied combinations lead to a value of λ_1 located around 31.5% (the maximum deviation from this central value being $\pm 0.2\%$), and that they mainly differ from each other by the value of λ_2. One can then conclude, as partially stated in the visual inspection, that the three-degree-of-freedom architectures SPH@CP and HPR@CP are the best performing. Note also that SPH@CG and HPR + HF are interesting compromises because of their intermediate results for both λ_1 and λ_2.

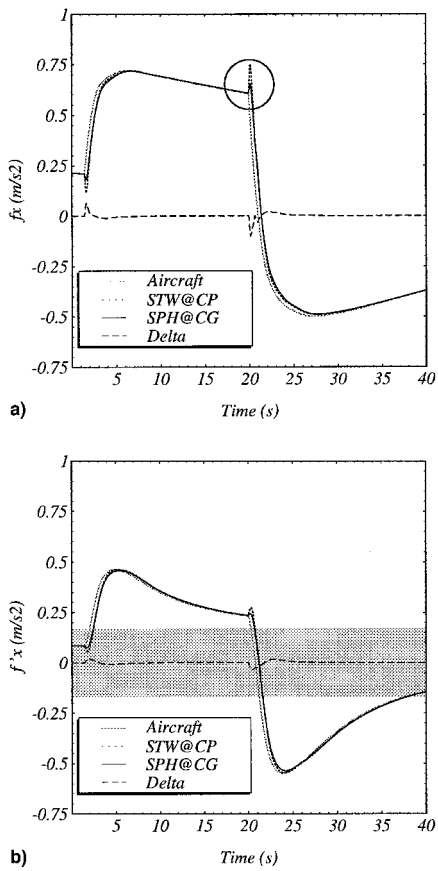

Fig. 8 Specific forces generated in the TIM. *x* component of a) *f* and b) *f'*.

TIM

This third maneuver takes place completely in a vertical plane and no lateral motions are sensed by the pilot. Moreover, this maneuver is the smoothest of the three studied here and contains only low-frequency motions. This therefore explains the excellent quality of simulation that was obtained with all of the simulators considered. Figure 8 shows the motion produced by SPH@CG and STW@CP. All three curves are almost superimposed for the entire maneuver.

This maneuver generates high-frequency accelerations only two times in its 40-s duration. These high-frequency accelerations lead to a half-second delay, which can be observed during the steep changes in f_X and f'_X. However, the more serious effects of these high-frequency accelerations are the sudden peaks (false cues) that are visible on the f_X curves produced by both simulators. This peak almost vanishes after being processed by the vestibular model. The false cues produced by the Stewart platform are almost three times worse than for the three-degree-of-freedom SPH motion base. In fact, the severity of these particular false cues is proportional to the length of $\boldsymbol{R}_0$ because they represent the translational acceleration induced by the angular acceleration at the onset of tilt coordination. Thus, no such peaks were observed in the @PH simulations where $\|\boldsymbol{R}_0\| = 0$. This fact is well represented in Fig. 6c, where two distinct clusters of combinations are obtained, the lowest of them being mainly composed of the @PH combinations.

Conclusions

This paper investigated the potential of a variety of three-degree-of-freedom motion platforms for the simulation of large transport aircraft motions. These platforms could be constructed and operated more economically than the present standard Stewart platform. In addition, such platforms might be appropriate for low-cost procedure training simulators or for entertainment applications. Two basic architectures, one with three rotational DOFs, the other with heave, pitch, and roll DOFs, were compared to the conventional Stewart platform. Variations in the washout location and the addition of a HF emulator were considered. In all, nine platform combinations were evaluated using three maneuvers. The comparison was mainly performed by visual inspection of graphical results, but objective performance indicators were also devised and used as a backup comparison tool.

The analysis of the results revealed that, in most cases, a three-degree-of-freedom simulator is capable of producing a simulation quality comparable to that obtained with the six-degree-of-freedom Stewart platform. The conclusions based on the vestibular model results do not differ appreciably from the ones based on motion time histories. In fact, it was usual to notice that the vestibular model processing increased the similarity between the three-degree-of-freedom and six-degree-of-freedom simulations. The following conclusions are based on these results:

1) Three-degree-of-freedom simulators represent a feasible alternative to six-degree-of-freedom motion systems because they can lead to a relatively good quality of simulation for large transport aircraft, such as the Boeing 747. Each of the motion degrees of freedom that were left unchanged, e.g., the angular velocities in the case of spherical mechanisms, produced identical motion histories. Maneuvers such as a TIM or TEM produced very similar results for all of the simulators because they involve low-frequency motions which can be well reproduced using primarily tilt coordination.

2) The most effective, versatile, and compliant three-degree-of-freedom architecture investigated here appears to be SPH@CG because it performed well in all three maneuvers.

In addition, the HPR@PH and SPH + HF performed well enough to deserve further investigation. These conclusions can also be derived by means of the Performance Indicators analysis.

3) The weak point of the three-degree-of-freedom simulators investigated here is their inherent incapability to simulate high-frequency translational accelerations. Although the pilot can be subjected to high-frequency specific forces if the vector $\boldsymbol{R}_0$ is nonzero, these motions are coupled to high-frequency angular accelerations. Thus, they cannot be controlled independently, in particular, when using a conventional washout filter algorithm.

4) Performing the washout at the pilot's head removes the spurious cues generated by washout artifices such as tilt coordination. However, it also obviates the possibility of using the HF emulator to simulate high-frequency translational accelerations in the three-degree-of-freedom motion bases.

5) The landing flare would also have been a relevant maneuver to simulate in this study because the motion cue (in heave) is particularly important. However, it has been omitted principally because no recordings of this maneuver were available. If that maneuver had been performed, it would likely have placed the SPH architecture at a disadvantage to the other two because of its lack of heave channel of motion.

Future work will entail test sessions with airline pilots on a real simulator (whose motion can be constrained to simulate a three-degree-of-freedom system), as well as the design of a three-degree-of-freedom simulator. It would also be of interest to develop a completely new washout algorithm, which could be optimized to achieve the best performance from a three-degree-of-freedom motion base.

Acknowledgments

The work reported here was funded by the Natural Sciences and Engineering Research Council of Canada under a Collaborative Projects Grant, and by a grant from the Ministry of International Affairs of the Government of Québec. Thanks are extended to Lloyd Reid for permission to use software developed at the University of Toronto Institute for Aerospace Studies.

References

[1]Crassous de Medeuil, C., "Évolution des Simulateurs d'Avions Civils," *Onde Électrique*, Vol. 68, No. 6, 1988, pp. 35–41.

[2]Lapiska, C., Ross, L., and Smart, D., "Flight Simulation. An Overview," *Aerospace America*, Vol. 31, No. 8, 1993, pp. 14–17, 33.

[3]Shibaev, V. M., "New Concept of the Motion System for the Low Cost Flight Simulator: Development and Design," *Proceedings of the 1993 AIAA Flight Simulation Technologies Conference*, AIAA, Washington, DC, 1993.

[4]Yang, P. H., Waldron, K. J., and Orin, D. E., "Kinematics of a Three-Degree-of-Freedom Motion Platform for a Low-Cost Driving Simulator," *Proceedings of the 5th Symposium on Advances in Robot Kinematics* (Portorož, Slovenia), Kluwer Academic, Dordrecht, The Netherlands, 1996, pp. 89–98.

[5]Repperger, D. W., "Study of Supermaneuverable Flight Trajectories Through Motion Field Simulation of a Centrifuge Simulator," *Journal of Dynamic Systems, Measurement and Control*, Vol. 114, No. 2, 1992, pp. 270–277.

[6]Leung, Y. M., "Solution of the General Flight Equations in Real Time," M.S. Thesis, Dept. of Aerospace and Engineering, Univ. of Toronto, Toronto, ON, Canada, 1985.

[7]Hanke, C. R., and Nordwall, D. R., "The Simulation of a Jumbo Jet Transport Aircraft, Volume II: Modeling Data," NASA CR-114494, Sept. 1970.

[8]Gum, D. R., "Modeling of the Human Force and Motion-Sensing Mechanisms," Air Force Human Resources Lab., TR-72-54, June 1972.

[9]Zacharias, G. L., "Motion Cue Model for Pilot-Vehicle Analysis," Aeronautical Maritime Research Lab., TR-78-2, May 1978.

[10]Reid, L. D., and Nahon, M. A., "Flight Simulation Motion-Base Drive Algorithms: Part 1—Developing and Testing the Equations," Univ. of Toronto, Inst. for Aerospace Studies, Rept. 296, ON, Canada, Dec. 1985.

[11]Nahon, M. A., Reid, L. D., and Kirdeikis, J., "Adaptive Simulator Motion Software with Supervisory Control," *Journal of Guidance, Control, and Dynamics*, Vol. 15, No. 2, 1992, pp. 376–383.

[12]Reid, L. D., and Nahon, M. A., "Flight Simulation Motion-Base Drive Algorithms: Part 2—Selecting the System Parameters," Univ. of Toronto, Inst. for Aerospace Studies, Rept. 307, ON, Canada, 1986.

[13]Reid, L. D., and Nahon, M. A., "Flight Simulation Motion-Base Drive Algorithms: Part 3—Pilot Evaluations," Univ. of Toronto, Inst. for Aerospace Studies, Rept. 319, ON, Canada, 1986.

[14]Reid, L. D., and Nahon, M. A., "Response of Airline Pilots to Variation in Flight Simulator Motion Algorithms," *Journal of Aircraft*, Vol. 25, No. 7, 1988, pp. 639–646.